

Monolithic Piezoelectric Insect with Resonance Walking

Shannon A. Rios¹, Andrew J. Fleming² and Yuen Kuan Yong³

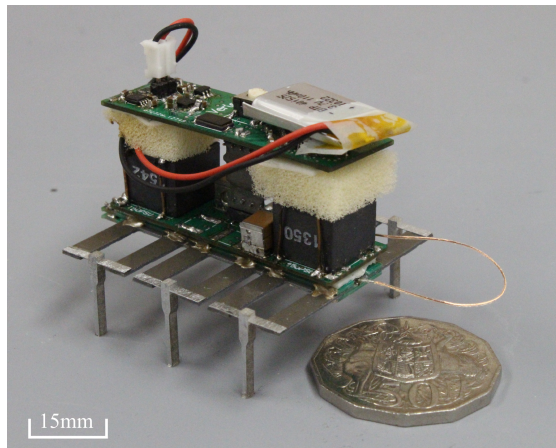


Fig. 1. MinRAR V2.

Abstract—This article describes the design, manufacture and performance of an untethered hexapod robot titled MinRAR V2. This robot utilizes a monolithic piezoelectric element, machined to allow for individual activation of bending actuators. The legs were designed so that the first two resonance modes overlap and therefore produce a walking motion at resonance. The monolithic construction significantly improves the matching of resonance modes between legs when compared to previous designs. Miniature control and high voltage driving electronics were designed to drive 24 separate piezoelectric elements powered from a single 3.7 V lithium polymer battery. The robot was driven both tethered and untethered and was able to achieve a maximum forward velocity of 98 mm/s when driven at 190 Hz and 6 mm/s at 5 Hz untethered. The robot is capable of a wide range of movements including banking, on the spot turning and reverse motion.

I. INTRODUCTION

Autonomous walking robots are complex machines comprised of many sensors, actuators and control electronics. Due to the complexity, significant challenges are involved with miniaturization. Construction methods and mechanics that work well in macro-scale robots may not be suitable for miniaturization due to the dominance of surface forces including friction [1]. By replacing standard mechanical components such as motors, bearings and other sliding joints with flexures and piezoelectric actuators, this problem can be mitigated.

There has been a wide variety of miniature robots developed over the past decade. For example, Wood *et al.* developed several miniature robots utilizing piezoelectric bender actuators for locomotion [2]–[6]. One such example is a 1.7 g hexapod robot that

The Authors are with the Precision Mechatronics Laboratory, School of Electrical Engineering and Computer Science at the University of Newcastle, Callaghan, NSW 2308, AUSTRALIA

¹Shannon.Rios@newcastle.edu.au

²Andrew.Fleming@newcastle.edu.au

³Yuenkuan.Yong@newcastle.edu.au

This work was performed in part at the University of Adelaide OptoFab node of the Australian National Fabrication Facility utilizing Commonwealth and It. SA State Government funding.

was able to achieve a forward travel speed of 0.9 body lengths per second [7]. This robot was approximately 4.8 cm long and consisted of three leg pairs where each pair of legs were driven by three piezoelectric benders arranged to amplify the displacement and produce a tripod gait.

Another example of a miniature piezoelectric robot is highlighted in the works of Oldham *et al.*. This work focused on the modeling, control and manufacture of multi-degree-of-freedom microrobotic legs that utilize thin-film PZT actuators [8], [9]. It is estimated that a robot using this form of actuator would achieve a forward locomotion speed of 27 mm/s. Additional work has characterized the effect of dynamic contact iterations on microrobotic leg structures [10].

Nguyen *et al.* have produced a tethered meso-scaled hexapod robot driven by ‘soft’ dielectric elastomer actuators [11]. The elastomer’s were segregated into four separate actuators able to produce three DoFs per leg. The constructed robot weighed approximately 80 g and was able to achieve a forward locomotion speed of 4 mm/s when driven with a 3.5 kV square wave at 0.5 Hz.

An example of a novel approach to miniature robotic locomotion can be seen in the works of Hariri *et al.* [12]–[14]. These works outline the design and development of a meso-scaled robot driven by a traveling wave in an aluminum beam. The traveling wave is excited by one or two piezoelectric patches at either end of an aluminum beam and the speed of the robot can be controlled by varying the amplitude of the voltage. Another robot developed by Hariri *et al.* uses a similar method to excite a standing wave on a legged robot [15]. These robots are able to achieve a forward locomotion speed of 246.5 mm/s and 40 mm/s respectively.

The work of Lee *et al.* shows a more extreme simplification of actuators and control [16]. Their work outlines a tethered miniature inchworm style robot that is driven by a single electromagnetic actuator. This robot can produce forward locomotion speeds of up to 36 mm/s and measures 12.2 mm x 11 mm x 9 mm in size and has a mass of 2.86 g.

The use of resonant vibration in miniature robotics was also reported by Becker *et al.* in their work on piezo-driven micro robots [17]. Their work outlines the development of a range of robots capable of traveling over both land and water. These robots used forced vibration to achieve two axis locomotion utilizing a single piezoelectric actuator.

As well as walking robots, piezoelectric actuators have also been applied to flying [18] and even swimming robots [19]. The work of L. Cen and A. Erturk describes a fish like autonomous robot that uses a macro-fiber composite, flexible piezoelectric actuator for propulsion. This robot was able to achieve an untethered swimming speed of up to 7.3 cm/s when driven with a 5 Hz actuation signal [19].

Similar principles that are applied to miniature robot actuators are also applied to a wide range of other piezoelectric actuators such as micro-grippers [20] and transducers [21]–[24]. The works of Fujun Wang *et al.* describe the design and control of a piezoelectric micro-gripper that uses a three-stage flexure-based amplification technique to achieve a large amplification factor of up to 22.6 [25].

This article describes the design, manufacture and performance of a monolithic miniature hexapod robot named MinRAR V2 and

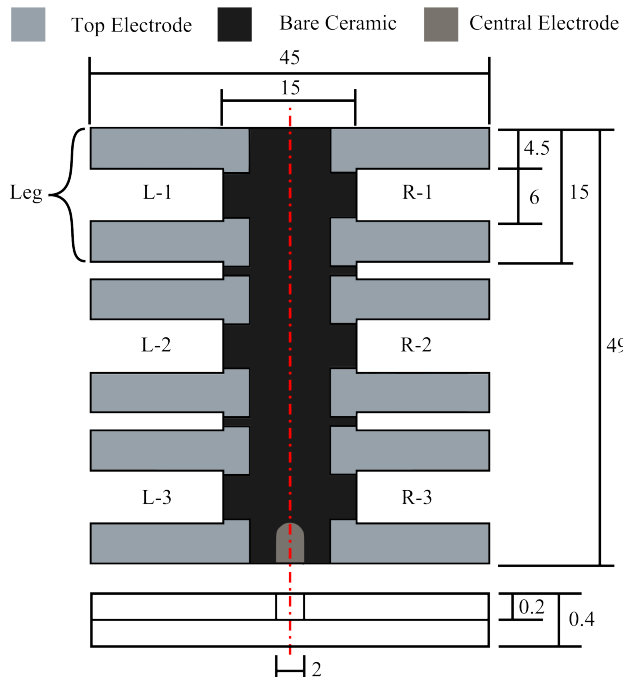


Fig. 2. Monolithic chassis. All dimensions given in mm.

shown in Figure 1. This work builds on previous research into the use of piezoelectric actuators in miniature robots described in [26]–[28] by improving the monolithic chassis construction techniques, refining the resonant leg design and by miniaturizing the control electronics to allow for un-tethered operation. The following section outlines the configuration of the robot and the mechanical modeling is discussed. Subsequently the electrical design and control methodology is described. Lastly the experimental results are discussed and the article is concluded with a comparison to existing miniature robots.

II. CONFIGURATION

The MinRAR V2 is a monolithic hexapod robot that uses a piezoelectric bimorph body and aluminum end-effectors to produce motion. The geometry of the body, shown in Figure 2, is similar to the previous monolithic robot described in [27] and is comprised of six legs that are driven with a tripod style gait to produce an ambulatory motion. The body was milled from a single sheet of 0.4 mm PZT-5A series poled bimorph supplied from Piezo Systems Inc. using an ultrasonic milling machine.

Differing from the MinRAR V1, the V2 is designed to be completely un-tethered and includes all control and power electronics as well as a small lithium polymer battery. Additionally, the monolithic chassis of the V2 lacks a central brass shim and the nickel electrodes were machined instead of etched. Removing the brass shim from the piezo elements improves the reliability of the machining process and by milling the electrodes during this machining process instead of etching them after simplifies the overall construction process. Also issues with resistive uniformity were removed when switching to milled instead of etched electrodes.

Each leg is comprised of two piezoelectric bimorph actuators mounted side-by-side and joined at their tips by a flexure and end-effector as per Figure 3. Motion can be achieved when the two benders are driven independently with a sinusoidal waveform and the phase difference between these drive signals determines the proportions of lifting and swinging that occur. This phase

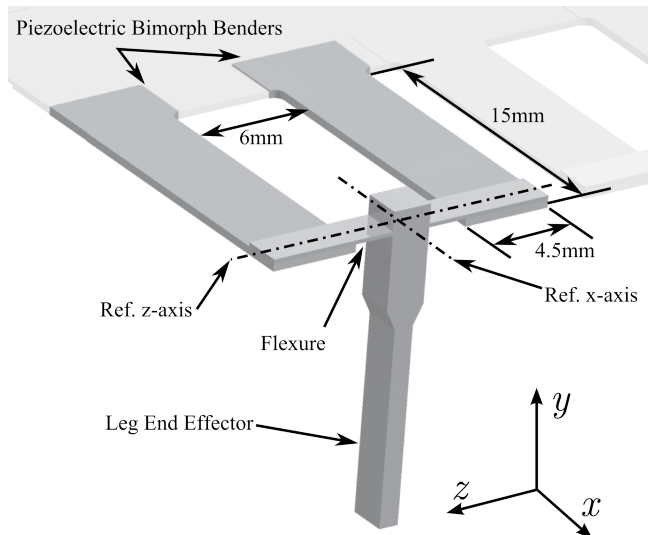


Fig. 3. Leg diagram.

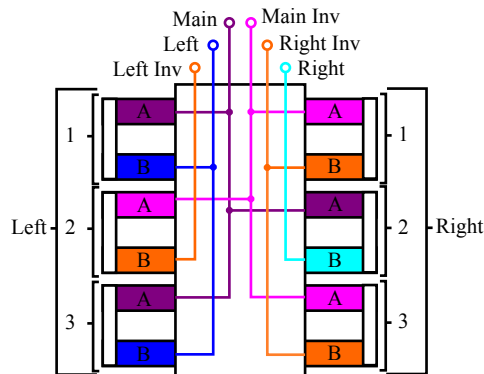


Fig. 4. Actuator wiring diagram.

difference is referred to as the ‘step-phase’ and a wide range of motions can be achieved by changing this, for example, when the two benders are driven in phase (0° step-phase), a lifting motion of the leg will be produced, similarly, when driven out of phase (step-phase of 180°) a swinging motion is produced. Nominally, a step-phase of 90° is used for walking as this produces equal proportions of lifting and swinging. Any step-phase between these two extremes will produce a combination of lifting and swinging. When the legs are driven with a step phase greater than 180° or less than 0° the motion will be reversed, in this way the robot can be made to walk backward or turn on the spot.

The actuators are controlled using the dual bipolar series electrical configuration, which drives the top and bottom piezoelectric electrodes 180° out of phase with each other and was chosen so that the central electrode, which is common between all actuators, can be grounded [29]. Using this method a total of six control signals are required to drive MinRAR V2, three primary drive signals (Main, Right and Left) and three inverse drive signals (Main Inv, Right Inv and Left Inv). Figure 4 shows the connection diagram for the top layer of the miniature robot and for the bottom layer, the signals are phase shifted by 180° .

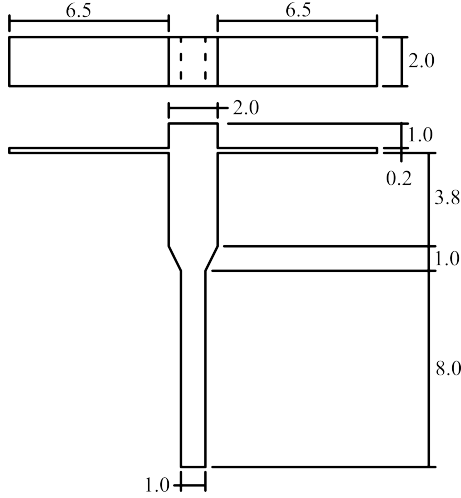


Fig. 5. Schematic of flexure and end-effector. All dimensions given in mm.

III. MECHANICAL DESIGN

Due to the unique geometry of the leg the first and second resonance modes are reasonably close together and produce a lifting and swinging motion respectively. By modifying a small set of parameters these two modes can be made to overlap and a combination of lifting and swinging will occur during resonance which produces a walking motion.

The primary method for controlling the resonance modes is to alter the lumped inertia of the end-effector and stiffness of the flexure. A set of equations, previously outlined in [28], describe a collection of single degree of freedom lumped mass models that can be used to approximate the resonance frequency for each DoF by finding the lumped inertia and stiffness and using $f = \frac{1}{2\pi} \sqrt{\frac{J}{I}}$. For the x-axis rotational DoF or ‘swinging’ DoF, the effective rotational stiffness (J_x) and rotational inertia (I_x) is,

$$J_x = \frac{J_{Fx}J_{Px}}{J_{Fx} + J_{Px}}, \quad I_x = I_{Px}B^2 + \frac{I_L}{2}, \quad (1)$$

$$B = \frac{J_{Fx}}{J_{Fx} + J_{Px}}, \quad (2)$$

where the subscripts F , P and L refer to the flexure, bender and leg respectively. The other DoF of interest is the rotation about the z-axis or ‘lifting’ DoF. The effective stiffness (J_z) and inertia (I_z) for this DoF is,

$$J_z = \frac{J_{Fz}J_{Pz}}{J_{Fz} + J_{Pz}}, \quad I_z = I_{Pz}C^2 + \frac{I_L}{2}, \quad (3)$$

$$C = \frac{J_{Fz}}{J_{Fz} + J_{Pz}}. \quad (4)$$

The specific equations for stiffness and inertia can be found in the authors previous work [28].

These models were used to design the flexure and end-effector such that the first resonance mode was above 500 Hz and the first and second resonance modes were within 50 Hz of each other. The end-effectors were machined from aluminum and glued to the robot body using a high strength two part epoxy. The final end-effector and flexure design is shown in Figure 5 and Table I shows the calculated stiffness and inertias. Using the lumped mass model, the lifting and swinging DoF resonances are 569 Hz and 595 Hz respectively.

Although these models provide a reasonable approximation of the system performance there are several effects that are ignored. These effects include: the stiffness added to the tip of the actuator

TABLE I
TABLE OF STIFFNESS AND INERTIA

Stiffness	
J_{Fx}	0.1056 Nm
J_{Fz}	0.0667 Nm
J_{Px}	0.0977 Nm
J_{Pz}	0.2326 Nm
K_y	6.0695 kN/m
Inertia	
I_{Px}	1.7039×10^{-8} kg.m ²
I_{Pz}	1.5398×10^{-9} kg.m ²
I_L	6.4065×10^{-9} kg.m ²

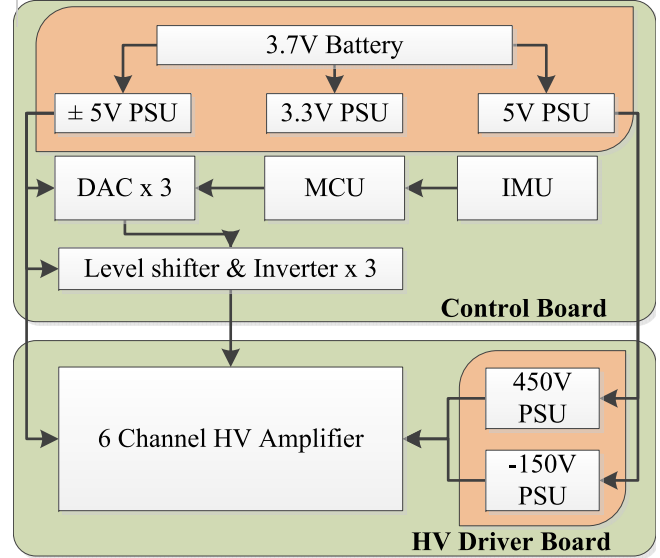


Fig. 6. Miniature controller block diagram, elements are as follows: PSU (Power Supply Unit), MCU (Microcontroller Unit), IMU (Inertial Measurement Unit), DAC (Digital-to-Analog Converter)

due to the glue and flexure, in-plane bending or twisting of the actuator and stretching of the flexure.

IV. ELECTRICAL DESIGN

Piezoelectric actuators require voltages on the order of 2000 V/mm in the polling direction and -500 V/mm in the reverse direction. The piezoelectric actuators on the MinRAR robot are approximately 0.2 mm thick and require a maximum forward driving voltage of 400 V and a maximum reverse voltage of -100 V. Typically this voltage is generated by large bench top power supplies, amplifiers and control electronics, however, these are too bulky for a miniature robot so a custom miniature controller must be designed.

A block diagram of the miniature controller is shown in Figure 6. The controller functionality is split between two PCBs, the ‘Control Board’ and the ‘HV Driver Board’. These boards are both 0.8 mm thick, four layer PCBs that measure 15 mm x 50 mm in area and are joined together through an 8-pin connector to transmits the six actuator control signals as well as power and ground for the high voltage supplies. The Control Board contains the battery and low voltage power supplies as well as the microcontroller, inertial measurement unit and analog IO circuitry. The HV Driver Board houses the two high voltage power supplies as well as the high voltage amplifiers that directly drive the piezoelectric actuators.

A. Power Design

This design uses a single 3.7 V, 110 mAh, lithium polymer battery as its energy source. The miniature controller requires several different voltages to operate including a 3.3 V power supply for the microcontroller and inertial measurement unit, a ± 5 V power supply for the digital to analog converter and a separate, high power 5 V supply for the HV Driver Board.

The HV Driver Board contains two miniature (12.5 mm x 12.5 mm) high voltage power supplies from Pico Electronics that produce the 450 V (Part No. 5SMV450) and -150 V (Part No. 5SMV150) DC voltages. These power supplies have a power output of 1.25 W each with a maximum efficiency between 70% to 76%. A 2.2 μ F capacitor was added to the output of these power supplies to improve their stability and remove potentially damaging voltage ripple.

The quiescent power consumption of the robot is 1.93 W. This was measured with a multimeter when the actuators were connected, but no driving signal being generated. With a 5 Hz driving signal, the power consumption increases to 2.35 W. This implies a figure of 84 mW of power consumption per hertz driving frequency. When the robot is driven at 5 Hz with a 110 mAh lithium polymer battery it will have a theoretical un-tethered operating time of 10 minutes, however once the battery voltage drops below 3.6 V the input current becomes too high and the 5 V supply will shutdown, so a practical working time of around 6-8 minutes is achieved.

The working time would be improved by increasing the capacity of the battery, however due to the size and dimensions of the robot it would be limited to approximately 15 mm x 50 mm in area. The mass of the battery would also effect the amount of lift that each leg achieves during a stride. Based on the y-axis stiffness of the legs given in Table I and an assumption of three legs in contact with the ground, approximately 0.53 μ m of displacement occurs in the y-axis per gram of robot weight, with the total lift height being approximately 100 μ m, the robot would be able to achieve efficient locomotion with up to 20% mass loading, equivalent 20 μ m of lost displacement or 80 μ m of total leg lift height. The deflection due to the mass (27.5 g) of the robot is approximately 14.84 μ m, therefore the battery or any additional payload for the robot should not exceed 10 g.

B. Digital Design

The control signals for the robot are generated by three single channel 12-bit DACs (Part No. MCP4725AOT-E/CH) which are serially controlled over i²c with an update rate of 10 kHz by an STM32L4 low power microprocessor. The DACs produce a 0-5 V output which is then level shifted down by 4 V to create a -4 to 1 volt control signal in addition to a complimentary 180 degree-out-of-phase signal. A 9-axis IMU with an accelerometer, gyro and magnetometer can also be used as a feedback sensor to adjust the robots position and heading.

C. High Voltage Amplifier

The high voltage amplifier, shown in Figure 7, is a low power amplifier with an input to output gain of -100 V/V. The MOSFETs are AO3162 with an SOT-23 footprint, similarly the BJT transistor is a PNP ZXTPO8400BFF in a SOT-23 package. The resistors and diodes are all 0603 and the capacitors are 0805 packages. The resultant amplifier fits into an area approximately 15 mm x 7.5 mm, making an extremely compact circuit.

A frequency response analysis was performed on the amplifier circuit by applying a 100 mV peak-to-peak pseudo random noise

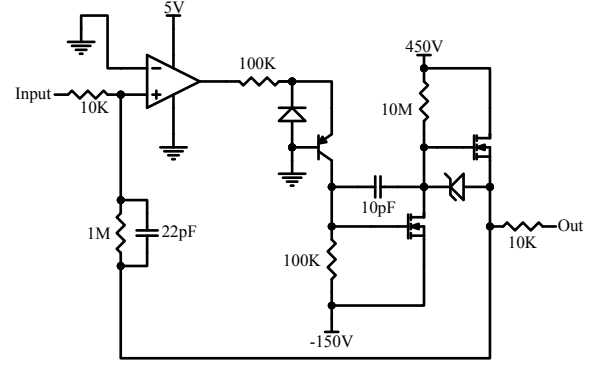


Fig. 7. High voltage amplifier circuit.

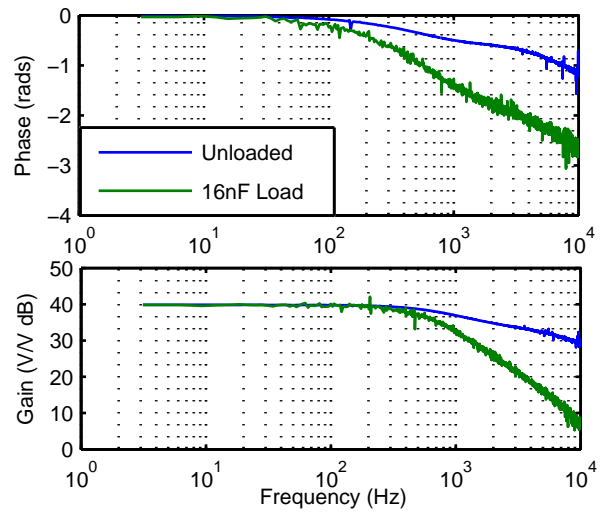


Fig. 8. Amplifier frequency response.

signal and captured using a SignalCalc Ace from Data Physics. The results for both the unloaded and loaded conditions are shown in Figure 8. The frequency response for the unloaded amplifier has a cut-off frequency of approximately 1 kHz and when loaded with a 16 nF capacitive load, the cut-off frequency is reduced to approximately 520 Hz.

The slew rate and quiescent power consumption for the amplifier were also measured. The maximum falling and rising slew rates were calculated by applying a square wave to the amplifier and measuring the slope of the respective edges. The rising and falling slew rates were 0.25 V/us and 2.16 V/us respectively. The quiescent current from the high voltage power supplies was approximately 81 μ A for the 450 V supply and 122 μ A for the -150 V supply. Using these figures the quiescent power consumption is approximately 54.75 mW per amplifier for a total quiescent power of 330 mW.

The maximum current for each amplifier was calculated to be 8.4 mA based on a maximum temperature rise of 100°C for the MOSFETs. Given a capacitance of between 5 nF and 6 nF per piezoelectric element and these power requirements, the maximum continuous driving frequency for the robot should not exceed 90 Hz to avoid amplifier failure, however this limit could temporarily be exceeded.

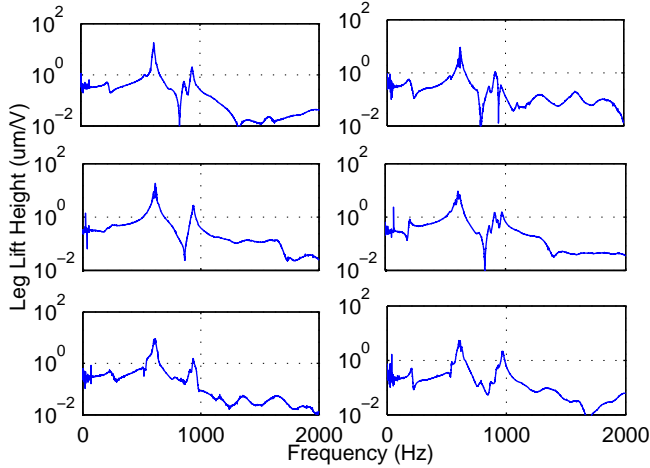


Fig. 9. Free air frequency response. From top to bottom, left to right, leg 1, left leg 2, left leg 3, right leg 1, right leg 2, right leg 3

V. EXPERIMENTAL RESULTS

The frequency response of each leg in free air was measured to find and compare the resonance modes. Next the ground contact frequency response was measured and finally the speed and turning capabilities of the robot are discussed.

A. Frequency Response Analysis

The frequency response analysis was performed by exciting the main driving actuators with a 4 V peak-to-peak pseudo random noise signal and measuring the velocity of the actuators using a polytec vibrometer. The analysis was performed while the robot was held in a 3D printed mount that restricted the lateral movement while allowing the legs to move freely with the laser mounted above. The magnitude response plots shown in Figure 9 identify an average first resonance of 604 Hz with a maximum of 613 Hz and a minimum of 600 Hz and an average second resonance of 615 Hz with a maximum of 620 Hz and a minimum of 613 Hz.

These figures align closely with the lumped mass model results but show a slightly stiffer system than predicted. This is most likely due to a stiffer mounting condition caused by the silver epoxy connecting the control board to the actuators and the high strength epoxy used to join the flexure to the actuators.

The ground contact frequency response for the robot was also identified and is shown in Figure 10. This frequency response was found using the same method as the free air response, however a platform was added so that the weight of the robot was fully supported by the legs while the robot was restricted from moving forward. Important features of this response are small resonances at 40 Hz, 65 Hz, 106 Hz, 180 Hz, 270 Hz and 435 Hz. Similar to the results published in previous work [28], ground contact significantly reduces the peaks of the frequency response and has the effect of shifting the resonances to a lower frequency. This is due to a change in the mounting conditions of the cantilever and more investigation is required to further study this effect. These lower frequency resonances are still seen to have a positive effect on the overall performance of the robot as shown by Figure 11.

B. Performance

To find the velocity to frequency relationship, the robot was filmed using a DSLR camera recording at 50 fps while being

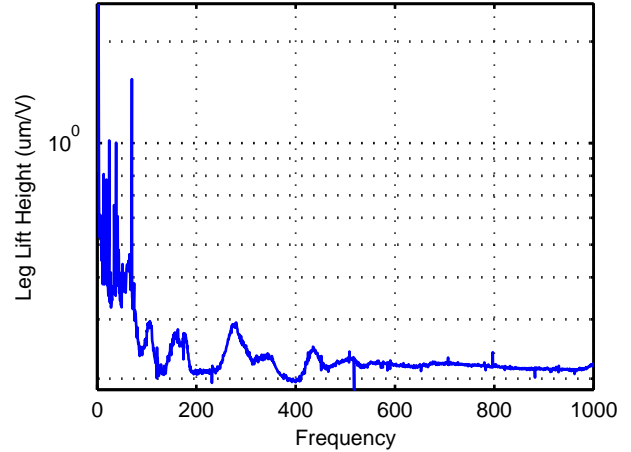


Fig. 10. Ground contact frequency response for left leg number 2.

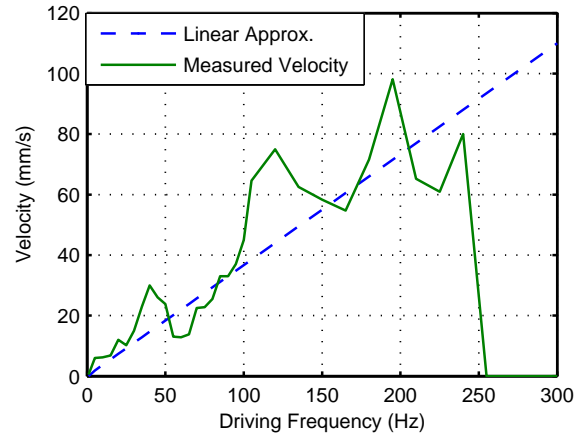


Fig. 11. Velocity vs Frequency curve.

driven with a +360 V to -90 V sine wave with a frequency from 1 Hz to 100 Hz in 5 Hz increments then from 100 Hz to 300 Hz in 15 Hz increments. The speed profile, shown in Figure 11, highlights a generally linear relationship with small resonances at 40 Hz, 110 Hz and 190 Hz which correspond well to the ground contact frequency response analysis. The velocity of the robot when driven with frequencies above 240 Hz is un-measurable due to destructive resonances that occur and overheating of the control electronics. An example of how the velocity was measured is shown in Figure 12.

The turning performance was measured by applying 180° out-of-phase driving signals to the left and right hand legs to force the left side of the robot to move forward, and the right side to move backwards, or *vice-versa*. By doing this the turning speed was determined to be approximately 12° per second when driven at a frequency of 5 Hz.

The performance of MinRAR V2 is compared to other similar style robots including the MinRAR V1 in Table II. The MinRAR V2 weighs approximately 30 g when loaded with a 110 mAh, 3.7 V lithium polymer battery. A maximum forward velocity of approximately 98 mm/s was achieved when driven at a frequency of 190 Hz. Although the MinRAR V2 was only able to achieve a maximum forward velocity of approximately one fifth that of MinRAR V1, it was able to achieve this with all required electronics

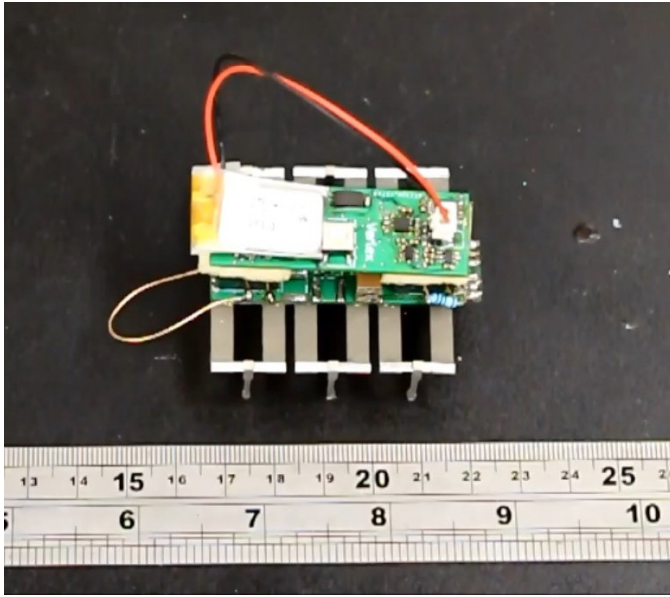


Fig. 12. Experimental Setup.

TABLE II
PERFORMANCE OF MINIATURE ROBOTS

Robot	Mass	Length	Max Speed	Tethered?
HAMR 3 [7]	1.7 g	48 mm	42 mm/s	No
Soft Robot [11]	80 g	182 mm	4 mm/s	Yes
m-DoF [9]	2.1mg/leg	-	27 mm/s	Yes
Hariri 1 [15]	3.25 g	50 mm	40 mm/s	Yes
LPMR [14]	6.27 g	50 mm	246.5 mm/s	Yes
MinRAR V1 [28]	16 g	55 mm	520 mm/s	Yes
MinRAR V2	28 g	55 mm	98 mm/s	No

onboard. It is important to note that some of these robots are self contained or un-tethered while others require external driving electronics and are tethered to an electrical supply, highlighted by the tethered column in Table II with yes for a tethered robot and no for a non-tethered robot.

VI. CONCLUSION & FUTURE WORK

The monolithic design of MinRAR V2 has improved the uniformity of the mechanical construction and therefore the performance of the robot. The robot was un-tethered and powered from a single cell 3.7 V lithium polymer battery. When driven at 5 Hz, it achieved a velocity of 6 mm/s and a turning speed of 12° per second.

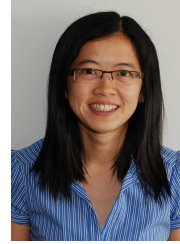
Due to the planar design of the chassis, the monolithic construction method results in a reduced leg lift height compared to MinRAR V1. This problem could be avoided by splitting the chassis along its length and angling each half upwards to gain increased leg lift height while still maintaining the advantages in uniformity of a monolithic design.

Future work will investigate the application of the resonance actuator to swimming and flying robots which operate in a more uniform environment. Additionally the miniature electronics will be improved to provide higher speed operation and increased efficiency by improving the high voltage DC-to-DC conversion process. MinRAR V2 can also be used as a test bed robot for a wide range of energy scavenging technologies including vibration harvesting and small scale PV cells. Lastly, by improving the

on-board sensors, miniature scale navigation and localization techniques will be investigated.



Shannon A. Rios Shannon A. Rios was granted a Bachelor of Electrical Engineering in 2012 from the University of Newcastle, Australia and later was awarded a Ph.D in Electrical Engineering in 2017 from the same institution. Shannon is currently working as an Engineering Design Teacher at Monash College. His research interests include miniature robotics, piezoelectric actuators and flying robotics. Dr Rios' was an Inventor on a patent application and received a nomination for best student paper at the 2015 IEEE AIM conference



Yuen Kuan Yong Yuen Kuan Yong received the Bachelor of Engineering degree in Mechatronics Engineering and the PhD degree in mechanical engineering from The University of Adelaide, Australia, in 2001 and 2007, respectively. She is an Australian Research Council DECRA Fellow with the School of Electrical Engineering and Computing, The University of Newcastle, Australia. Her research interests include nanopositioning systems, micro-cantilevers, high-speed atomic force microscopy, and miniature robotics. A/Prof Yong's research awards include the University of Newcastle Vice-Chancellor's Award for Research Excellence in 2014, and the Vice-Chancellor's Award for Research Supervision Excellence in 2017. She is an Associate Editor for the IEEE/ASME Transactions of Mechatronics, and Frontiers in Mechanical Engineering.



Andrew J. Fleming Andrew J. Fleming graduated from The University of Newcastle, Australia (Callaghan campus) with a Bachelor of Electrical Engineering in 2000 and Ph.D in 2004. He is presently a professor and Director of the Precision Mechatronics Lab at The University of Newcastle, Australia. His research interests include lithography, nano-positioning, scanning probe microscopy, and biomedical devices. Prof Fleming's research awards include the ATSE Batherham Medal in 2016, the IEEE Control Systems Society Outstanding Paper Award in 2007, and The University of Newcastle Researcher of the Year Award in 2007. He is the co-author of four books and more than 200 Journal and Conference articles. Prof Fleming is the inventor of several patent applications, and in 2012 he received the Newcastle Innovation Rising Star Award for Excellence in Industrial Engagement.

REFERENCES

- [1] W. S. N. Trimmer, "Microrobots and micromechanical systems," *Sensors and actuators*, vol. 19, no. 3, pp. 267–287, 1989.
- [2] R. Sahai, S. Avadhanula, R. Groff, E. Steltz, R. Wood, and R. S. Fearing, "Towards a 3g crawling robot through the integration of microrobot technologies," in *2006 IEEE International Conference on Robotics and Automation (ICRA)*, Orlando: IEEE, 2006, pp. 296–302.
- [3] M. Kovac, M. Bendana, R. Krishnan, J. Burton, M. Smith, and R. J. Wood, "Multi-stage micro rockets for robotic insects," in *Robotics: Science and Systems VIII*. MIT Press, 2013, p. 185.
- [4] A. T. Baisch, P. S. Sreetharan, and R. J. Wood, "Biologically-Inspired Locomotion of a 2g Hexapod Robot," in *International Conference on Intelligent Robots and Systems*, Taipei, 2010, pp. 5360–5365.
- [5] J. P. Whitney and R. J. Wood, "Conceptual design of flapping-wing micro air vehicles," *Bioinspiration & biomimetics*, vol. 7, no. 3, p. 036001, sep 2012.
- [6] K. Y. Ma, P. Chirattananon, S. B. Fuller, and R. J. Wood, "Controlled flight of a biologically inspired, insect-scale robot." *Science (New York, N.Y.)*, vol. 340, no. 6132, pp. 603–7, may 2013.
- [7] A. T. Baisch, C. Heimlich, M. Karpelson, and R. J. Wood, "HAMR3: An autonomous 1.7 g ambulatory robot," in *Intelligent Robots and Systems (IROS), 2011 IEEE/RSJ International Conference on*, San Francisco, 2011, pp. 5073–5079.
- [8] B. Edamana and K. R. Oldham, "Optimal Low-Power Piezoelectric Actuator Control With Charge Recovery for a Microrobotic Leg," *IEEE/ASME Transactions on Mechatronics*, vol. 18, no. 1, pp. 251–262, feb 2013.
- [9] C.-H. Rhee, J. S. Pulskamp, R. G. Polcawich, and K. R. Oldham, "Multi-degree-of-freedom thin-film PZT-actuated microrobotic leg," *Journal of Microelectromechanical Systems*, vol. 21, no. 6, pp. 1492–1503, 2012.
- [10] J. H. Ryou and K. R. Oldham, "Dynamic characterization of contact interactions of micro-robotic leg structures," *Smart Materials and Structures*, vol. 23, no. 5, p. 55014, 2014.
- [11] C. T. Nguyen, H. Phung, H. Jung, U. Kim, T. D. Nguyen, J. Park, H. Moon, J. C. Koo, and H. R. Choi, "Printable monolithic hexapod robot driven by soft actuator," in *2015 IEEE International Conference on Robotics and Automation (ICRA)*. Seattle: IEEE, 2015, pp. 4484–4489.
- [12] H. Hariri, Y. Bernard, and A. Razek, "A traveling wave piezoelectric beam robot," *Smart Materials and Structures*, vol. 23, no. 2, p. 25013, 2013.
- [13] —, "Dual piezoelectric beam robot: The effect of piezoelectric patches positions," *Journal of Intelligent Material Systems and Structures*, vol. 26, no. 18, pp. 2577–2590, 2015.
- [14] H. H. Hariri, L. A. Prasetya, G. S. Soh, S. Foong, K. Otto, and K. Wood, "A tether-less legged piezoelectric miniature robot using bounding gait locomotion for bidirectional motion," *2016 IEEE International Conference on Robotics and Automation (ICRA)*, pp. 4743–4749, 2016.
- [15] H. H. Hariri, G. S. Soh, S. H. Foong, K. L. Wood, and K. Otto, "Miniature Piezoelectric Mobile Robot driven by Standing Wave," in *Proceedings of the 14th IFToMM World Congress*, Stockholm, 2015, pp. 325–330.
- [16] K.-m. Lee, Y. Kim, J. K. Paik, and B. Shin, "Clawed Miniature Inch-worm Robot Driven by Electromagnetic Oscillatory Actuator," *Journal of Bionic Engineering*, vol. 12, no. 4, pp. 519–526, 2015.
- [17] F. Becker, "Piezo-driven Micro Robots for Different Environments: Prototypes and Experiments," in *Robotik 2012*, Munich, 2012, pp. 41–45.
- [18] R. Wood, R. Nagpal, and G.-Y. Wei, "Flight of the Robobees," *Scientific American*, vol. 308, no. 3, pp. 60–65, feb 2013.
- [19] L. Cen and A. Erturk, "Bio-inspired aquatic robotics by untethered piezohydroelastic actuation," *Bioinspiration & biomimetics*, vol. 8, no. 1, p. 016006, 2013.
- [20] F. Wang, C. Liang, Y. Tian, X. Zhao, and D. Zhang, "Design of a piezoelectric-actuated microgripper with a three-stage flexure-based amplification," *IEEE/ASME Transactions on Mechatronics*, vol. 20, no. 5, pp. 2205–2213, 2015.
- [21] H. Tzou, "Development of a light-weight robot end-effector using polymeric piezoelectric bimorph," in *Robotics and Automation, 1989. Proceedings., 1989 IEEE International Conference on*. IEEE, 1989, pp. 1704–1709.
- [22] Y. Li and Q. Xu, "Design and robust repetitive control of a new parallel-kinematic xy piezostage for micro/nanomanipulation," *IEEE/ASME Transactions on Mechatronics*, vol. 17, no. 6, pp. 1120–1132, 2012.
- [23] F. Wang, X. Zhao, D. Zhang, and Y. Wu, "Development of novel ultrasonic transducers for microelectronics packaging," *Journal of materials processing technology*, vol. 209, no. 3, pp. 1291–1301, 2009.
- [24] F. Wang, H. Zhang, C. Liang, Y. Tian, X. Zhao, and D. Zhang, "Design of High-Frequency Ultrasonic Transducers With Flexure Decoupling Flanges for Thermosonic Bonding," *IEEE Transactions on Industrial Electronics*, vol. 63, no. 4, pp. 2304–2312, 2016.
- [25] F. Wang, C. Liang, Y. Tian, X. Zhao, and D. Zhang, "Design and control of a compliant microgripper with a large amplification ratio for high-speed micro manipulation," *IEEE/ASME Transactions on Mechatronics*, vol. 21, no. 3, pp. 1262–1271, 2016.
- [26] S. A. Rios, A. J. Fleming, and Y. K. Yong, "Design of a two degree of freedom resonant miniature robotic leg," in *Advanced Intelligent Mechatronics (AIM), 2015 IEEE International Conference on*, Busan, jul 2015, pp. 318–323.
- [27] —, "Design and characterization of a miniature monolithic piezoelectric hexapod robot," in *Advanced Intelligent Mechatronics (AIM), 2016 IEEE International Conference on*. Banff: IEEE, 2016, pp. 982–986.
- [28] —, "Miniature Resonant Ambulatory Robot," *IEEE Robotics and Automation Letters*, vol. PP, no. 99, pp. 1–1, 2016.
- [29] S. A. Rios and A. J. Fleming, "A new electrical configuration for improving the range of piezoelectric bimorph benders," *Sensors and Actuators A: Physical*, vol. 224, pp. 106–110, 2015.